



Seismic reflection along the path of the Mediterranean Undercurrent

G.G. Buffett^{a,*}, B. Biescas^b, J.L. Pelegrí^c, F. Machín^c, V. Sallarès^b, R. Carbonell^a, D. Klaeschen^d, R. Hobbs^e

^a Institut de Ciències de la Terra “Jaume Almera”, C. Lluis Solé i Sabarís s/n, 08028 Barcelona, Spain

^b Unitat de Tecnologia Marina, CSIC, Passeig Marítim de la Barceloneta 37-49, 08003 Barcelona, Spain

^c Institut de Ciències del Mar, CSIC, Passeig Marítim de la Barceloneta 37-49, 08003 Barcelona, Spain

^d Leibniz-Institute of Marine Sciences, IFM-GEOMAR, Duesternbrooker Weg 20, D-24105 Kiel, Germany

^e Department of Earth Sciences, Durham University, Durham, DH1 3LE, UK

ARTICLE INFO

Article history:

Received 31 October 2008

Received in revised form

25 May 2009

Accepted 29 May 2009

Available online 10 July 2009

Keywords:

Seismic oceanography

Mediterranean Undercurrent

Thermohaline fine structure

Mixing

Entrainment

Temperature

Salinity

Amplitude

ABSTRACT

Seismic reflection profiling is applied to the study of large scale physical oceanographic processes in the Gulf of Cádiz and western Iberian coast, coinciding with the path of the Mediterranean Undercurrent. The multi-channel seismic reflection method provides clear images of thermohaline fine structure with a horizontal resolution approximately two orders of magnitude higher than CTD casting. The seismic data are compared with co-located historical oceanographic data. Three seismic reflectivity zones are identified: North Atlantic Central Water, Mediterranean Water and North Atlantic Deep Water. Seismic evidence for the path of the Mediterranean Undercurrent is found in the near-slope reflectivity patterns, with rising reflectors between about 500 and 1500 m. However, the core of the undercurrent is largely transparent. Seismic images show that central and, particularly, intermediate Mediterranean Waters have fine structure coherent over horizontal distances of several tens of kilometers. However, the intensity of the reflectors, and their horizontal coherence, decreases downstream. This change in seismic reflectivity is probably the result of diminished vertical thermohaline contrasts between adjacent water masses, so that double-diffusion processes become unable to sustain temperature and salinity staircases. Comparison of root-mean-square seismic amplitudes with temperature and salinity differences between the Mediterranean Undercurrent and the overlying central waters suggests a causal relationship between observed thermohaline fine structure and true seismic amplitudes. We estimate that, within this intermediate water stratum, impedance contrasts are mainly controlled by sound speed contrasts (a factor between 3.5 and 10 times larger than density contrasts), which are mainly controlled by temperature contrasts (a factor between 1.5 and 5 times larger than salinity contrasts).

© 2009 Elsevier Ltd. All rights reserved.

1. Introduction

Seismic reflection profiling is unique in its application to oceanography because of its method of implementation. Its low acoustic frequency, yet high level of lateral sampling allows oceanographers to create a quasi ‘snapshot’ of the ocean to visualize rapid changes in density and/or sound speed, which results in the identification of constant-property surfaces and their coherence over large horizontal distances. The multi-channel seismic reflection method (MCS) has been shown to be well suited to analyze the nature of thermohaline fine structure for many processes, from internal waves to frontal regions, with a lateral resolution of approximately two orders of magnitude greater than conventional oceanographic data (Ruddick, 2003; Thorpe, 2005).

Although acoustic probing of the ocean in various ways has been commonplace for decades, the first applications of seismic reflection profiling to the ocean were done by Gonella and Michon (1988) and Phillips and Dean (1991). These works, followed by the influential work of Holbrook et al. (2003) and subsequent studies (Biescas et al., 2008; Holbrook and Fer, 2005; Nakamura et al., 2006; Nandi et al., 2004; Páramo and Holbrook, 2005; Tsuji et al., 2005; Wood et al., 2008), have refined the seismic reflection ‘common mid-point’ (CMP) method to remotely image the ocean on a large scale—to full ocean depths and horizontally on the order of hundreds of kilometers.

Mediterranean Water (MW) enters the Atlantic Ocean through the Strait of Gibraltar as a result of the overflow of dense, saline water from the Mediterranean Sea, in the so-called Mediterranean Undercurrent (MU) (Bower et al., 2002). Guided by buoyancy and seafloor bathymetry the MU cascades down into the Gulf of Cádiz and mixes with North Atlantic Central Water (NACW) (Johnson et al., 1994) until it equilibrates at depths between 500 and 1500 m (Richardson et al., 2000), confined between the NACW and

* Corresponding author. Tel.: +34 93 409 5410; fax: +34 93 411 0012.

E-mail addresses: gbuffett@ija.csic.es, gbuffett@gmail.com (G.G. Buffett).

the North Atlantic Deep Water (NADW). Due to the Coriolis effect, the MU flows attached to the western continental slope of Iberia (Ambar et al., 1999) all the way into the Bay of Biscay and along the Porcupine Banks. Ochoa and Bray (1991) applied inverse methods to several sections in the Gulf of Cádiz to determine the existence of intense two-way mixing and one-way entrainment. Mixing, however, does not stop there because MW is progressively diluted along its path (Iorga and Lozier, 1999).

Near the Strait of Gibraltar the MU has a high thermohaline contrast and mixing may result from shear mixing (Price et al., 1993), while further downstream mixing may be the result of double-diffusive processes (Ruddick, 1992; Schmitt, 1994). The background upper-thermocline NACW becomes layered as a result of double-diffusion salt-fingering (St. Laurent and Schmitt, 1999). The MU intrusion causes salt fingering to be enhanced at the base of the MW, especially in the form of lateral intrusions (Ruddick, 1992; Ruddick and Kerr, 2003). MU intrusions also bring about the possibility of a diffusive regime on top of the MW intrusion (Ruddick and Gargett, 2003; Schmitt, 1994). We expect that these processes act all together and with different intensities resulting in a variety of thermohaline structures that change along the MU path.

Here we analyze seismic data for several normal-to-shore sections situated along the path of the MU, in order to investigate how inner-ocean reflectors evolve with distance from the source of MW, in the Strait of Gibraltar. These sections are examined in combination with historical, co-located CTD data, to appreciate how changes in these reflectors may respond to progressive mixing of MW in the North Atlantic Ocean.

2. Methodology

Since Obukhov (1941) there have been numerous treatises on acoustic methods to measure ocean fluid dynamic properties (Batchelor, 1957; Brandt, 1975; Chernov, 1957; Goodman, 1990; Munk and Garrett, 1973; Ottersten, 1969; Tatarski, 1971). Brandt (1975) studied high-frequency sound scattering from density variations of a turbulent saline jet in the laboratory. He concluded that the observed scattering was a result of acoustic impedance fluctuations produced by the jet and hence, that acoustic imaging techniques could be used to study oceanic diffusion processes and thermohaline structures. Orr and Hess (1978) acquired a joint physical oceanography/multifrequency (high-frequency) acoustic backscatter dataset. They observed that the intensity of back scatter was higher where the temperature gradient was maximum. They therefore suggested that oceanic microstructure played a role. Following this work, Haury et al. (1983) provided further constraints on the relationship between oceanic microstructure and acoustic backscatter. By combining the methods of Orr and Hess with plankton measurement constraints, they were able to produce an acoustic snapshot of an ostensibly breaking internal wave, thereby identifying thermohaline fine structure as the source of the backscatter. Munk and Wunsch (1979) first used travel-time ocean acoustic tomography by adapting a technique used in seismology to image the interior of the earth to represent very large scale ocean structures.

2.1. Seismic acquisition

The seismic acquisition survey was carried out in August and September 1993 to study the Iberian–Atlantic Margin (IAM) tectonic plate boundary (González et al., 1996). It proceeded by towing an impulsive source and a streamer (a cable filled with hydrophones), which recorded both signal and noise. The survey design and acquisition parameters were customized to the study of deep crustal structures. Nonetheless, the high energy source

and narrow receiver spacing provides a rich seismic oceanography dataset (Fig. 1). In this work we have analyzed four seismic profiles, chosen to intersect perpendicularly with the known path of the MU (Bower et al., 2002; Richardson et al., 2000; Serra and Ambar, 2002) at different distances from its origin, in the Gibraltar Strait. The first profile is located nearly 400 km west of the Strait of Gibraltar while the distance between adjacent transects is about 200 km.

Source generated seismic waves travel through the water column. Acoustic impedance boundaries defined by varying density and sound speed modify the transmission to reflection ratio. As a result, the changes in density and sound speed partially backscatter propagating acoustic energy. The imaging procedure (Sheriff and Geldart, 1982; Yilmaz, 1987), takes advantage of the redundancy of sources and receivers to produce a continuous image of the subsurface and to attenuate random noise. In this method, instead of a single source and receiver, there are many sequentially fired sources and an array of receivers at regular intervals with varying source–receiver offsets.

In terms of imaging the solid earth, a seismic reflection profile is effectively a ‘snap-shot’ in time (due to the enormous time involved in geological processes). However, in application to physical oceanography, the seismic section is skewed in time due to the dynamic nature of ocean current velocities, which circulate in a time comparable to seismic data acquisition resulting in a picture of a progressively changing ocean. Recent seismic studies have shown that subtle thermohaline fine structure changes can occur in as little as 3 h (Géli and Cosquer, in preparation). Detailed acquisition parameters are summarized in Table 1.

Vertical resolution is much lower than the resolution available in oceanographic in situ probing (e.g. CTD) and is determined by the frequency content of the source, how sound is filtered by the water column and, ultimately, by what frequency bandwidth is recorded. Widess (1973) defined a one-quarter wavelength relationship for seismic data, whereby the smallest resolvable interface is expressed as one-quarter of the dominant seismic wavelength. Therefore, given a dominant frequency of 50 Hz, structures no smaller than about 7.5 m are resolvable. In practice however, one-quarter wavelength resolution is not obtainable due to the thickness and sharpness of the reflecting interface. Thus, we can confidently image interfaces of only about one-half the dominant frequency, or 15 m for a 50 Hz dominant frequency. As a result, although scattering and reflection of acoustic waves is known to occur from biological sources, plankton for instance (Haury et al., 1983; Stanton et al., 1996), seismic acoustic sources produce lower frequency waves that are not sensitive to these organisms.

2.2. Seismic data processing

The Iberian–Atlantic Margin lines were processed and analyzed similarly (with the exception of particular dataset dependent parameters) to ensure consistent interpretation from line to line. The linear direct wave (the wave which travels directly from source to receiver without reflecting) is shown emanating from the source at the surface and becoming deepest at the farthest offset. The acoustic reflections are hyperbolic and have lower amplitudes than the direct wave. Since this is a shot from a marine survey, we see water column reflections, seafloor reflections and those beneath the seafloor (Fig. 2).

The ultimate goal of seismic data processing is to produce an accurate, interpretable zero-offset section. All recorded seismic data contain signal and noise. To increase the interpretability of seismic data, it is necessary to increase the signal-to-noise ratio. Noise can be present in the form of random or coherent noise.

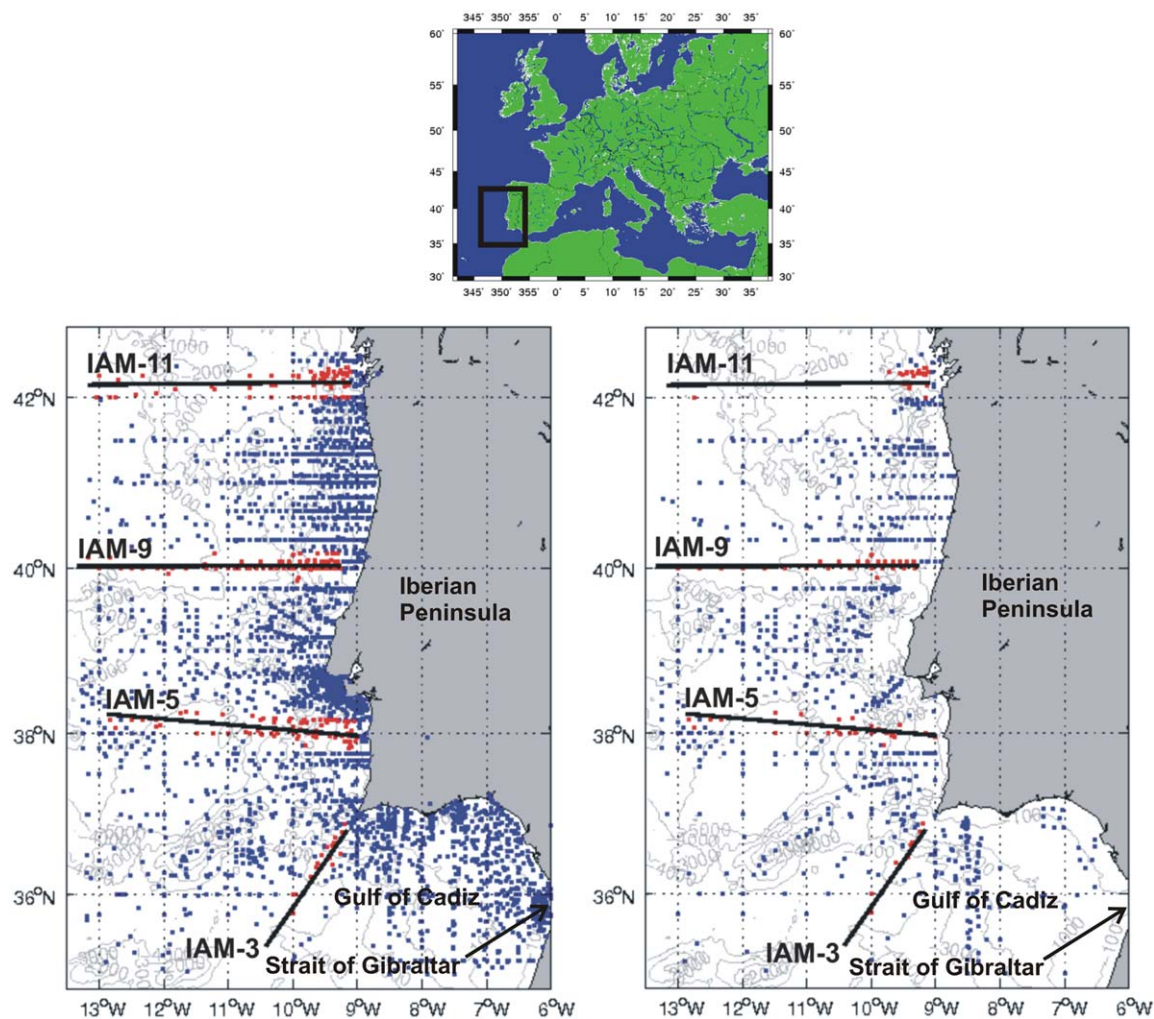


Fig. 1. Study location map showing seismic lines and oceanographic stations. Both databases supply quality-controlled data acquired throughout the 20th century. IAM sections are indicated. Stations within 20 km from these sections (red color) are used to build characteristic temperature and salinity fields. Left panel: WOD05 database (<http://www.nodc.noaa.gov/OC5/SELECT/dbsearch/dbsearch.html>). Right panel: Coriolis database (http://www.coriolis.eu.org/cdc/data_selection.htm).

Table 1
IAM Acquisition Parameters—the streamer used was the HSSQ/GX600 analog model.

Energy source—SWAG air gun array (bolt)
Total volume: 0.123 m ³
Nominal source depth: 10 m
Nominal shotpoint interval: 75 m
Peak energy: 20–50 Hz
Instrumentation—type: DFS-V
Format: SEG-D
Sample rate: 4 ms
Record length: 25 s
Low-cut filter OUT
High-cut filter 90 Hz
Cable Configuration—no. groups = 192
Streamer length: 5 km
Group interval: 25 m
Nominal cable depth: 15 m
Near offset (in-line): 254 m
CMP spacing: 12.5 m

The air gun array consisted of 36 BOLT guns organized into six identical sub strings.

While random noise is greatly reduced in the process of stacking (in the CMP method), due to the inherent redundancy of data traces, coherent noise has to be identified and attenuated to better

enhance the reflection signal. In the case of seismic oceanography, the direct wave is the most prominent coherent noise and strongly masks shallow reflections.

We used an eigenvector filter to suppress the majority of direct wave energy and as a result enhance reflections. This filter, based on the Kahrnen–Loeve transform (Jones and Levy, 1987), decomposes the seismic traces into eigen-images. To suppress the direct wave, the shot record was first flattened using a linear moveout (LMO) correction with a constant sound speed of 1505 m s^{−1}. The eigenvector filter was applied and the LMO correction removed (Fig. 2) (Claerbout, 1978; Yilmaz, 1987). An Ormsby band-pass filter was then applied, truncating the frequency range to between 15 and 90 Hz, to increase the signal-to-noise ratio, with tapered ends (8/15–90/100 Hz) to prevent discontinuities such as oscillatory edge effects.

Next, a correction for divergence energy loss (geometric spreading) was applied that operates on the basis of an inverse distance, 1/*r*, relationship. This cylindrical spreading correction assumes that the majority of energy comes from directly below the source, as opposed to off-line, as if energy propagates on a 2D vertical surface. This contrasts with spherical divergence corrections for 3D surveys, that would use a 1/*r*² relationship. A single trace scalar was applied to balance trace amplitudes for display purposes. This trace scalar balanced all samples in a trace by the same scalar value, as opposed to scalars which are calculated in a

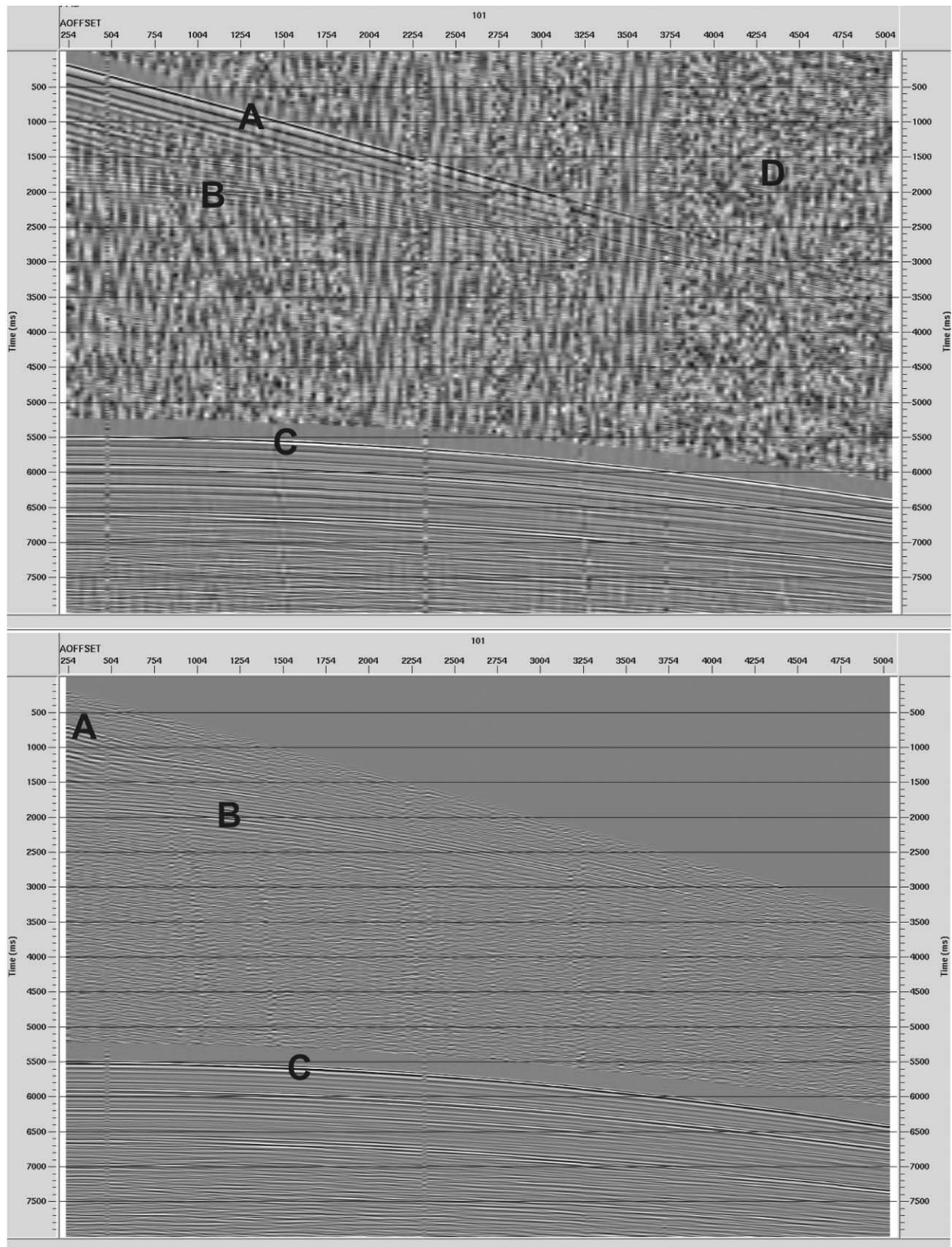


Fig. 2. Typical shot record from one IAM profile (IAM-3, SHOT 101) showing seismic events. (A) Direct wave. (B) Water column reflections. (C) Seafloor reflection. (D) Random noise. The shot record on the top shows the high amplitude direct wave (that masks lower amplitude water column reflections) and significant random noise. After application of the eigenvector filter, the direct wave is largely suppressed, with the exception of some residual energy at near offsets. The eigenvector filter is also very effective in reducing random noise.

sliding time window. In this way, lateral variations in amplitude are better preserved for data visualization. For true amplitude analysis (Section 3.2), no trace scalar was applied.

For a given CMP gather, in order to correct for the effect of normal moveout (NMO), that is, the effect of increasing reflection travel time to longer offset receivers, one needs to apply an appropriate shift in sound speed (known as ‘stacking velocity’) to flatten the hyperbolic reflectors (Hatton et al., 1986). In the water column, sound speed does not vary greatly, and indeed an assumed constant sound speed of 1500 m s^{-1} will produce a stack (zero-offset section), yet velocity (sound speed) analysis is necessary and does improve the final stacked section, especially in the shallow ocean, where interfaces are more sensitive to processing sound speed adjustments (Fig. 3). Traces were then stacked, the process of summing together traces. This process increases coherent signal and attenuates random noise. Post-stack processing included an f - x deconvolution to improve signal-to-noise ratio (Cowen and Grant, 1985; Treitel, 1974).

Following post-stack noise reduction, a phase-shift time migration was applied to move reflectors to their true spatial locations and to collapse diffraction artifacts (Gazdag, 1978). Migration makes an adjustment of dipping interfaces but requires a priori knowledge of the acoustic structure of the media in question. In practice (in the absence of co-located and simultaneously recorded in situ oceanographic sound speed measurements) this is not known and must be arrived at iteratively through ‘velocity analysis’. These fine depth variations are better sampled with oceanographic instruments and then used as the basis for seismic velocity analysis (that is, which sound speed function gives the best seismic stacking response). The result is a profile in two-way-time (vertical travel time to a reflection event and back) and horizontal distance. The two-way time profiles were converted to depth using the interval sound speed function calculated from picked stacking velocities using the Dix equation (Yilmaz, 1987). Fig. 3 illustrates the improved structural clarity obtained after velocity analysis. This is an important result, given the relatively small variations in water column sound speed as compared with those found in the solid earth.

2.3. Oceanographic data

Oceanographic data from 35°N to 42.5°N and 6°W to 13.5°W have been extracted from two historical databases: World Ocean Database 05 (WOD05) and Coriolis (Fig. 1a and b). Since most stations are present in both databases, some effort has been made

to identify and delete duplicate stations. Stations acquired at the same time within 0.01° in latitude and longitude are considered to be duplicates (such a radius is larger than the usual precision in navigation systems, but short enough to distinguish between two different, yet proximally located stations). The number of stations available for each IAM section is 16 (IAM-3), 55 (IAM-5), 115 (IAM-9) and 58 (IAM-11). It is important to note that these stations, separated by an average distance that varies between 10 and 20 km, are not simultaneous in time (to one another, nor to their respective seismic profiles). Rather, the stations come from many different years and seasons, so the ensembled oceanographic sections in Fig. 1 cannot be used to examine any sort of horizontal coherence. Nevertheless, they are useful to illustrate the distribution of water masses along the path of the MU. Moreover, the outflow of MW from the Strait of Gibraltar does not experience substantial seasonal or interannual changes (Ambar et al., 2002; Candela, 2001), so we may expect that the large-scale characteristics of the MU, including its path and the characteristics of its exchange with the surrounding North Atlantic waters, are largely invariant.

NACW salinity decreases monotonically with depth from a sea-surface maximum value, until reaching the influence of MW. In the absence of North Atlantic intermediate waters (such as MW or Antarctic Intermediate Water, AAIW) salinity decreases rapidly with depth in the upper-thermocline until it becomes roughly constant at intermediate water levels (e.g. Machín et al., 2006, Fig. 3). Off the Iberian Peninsula, however, the presence of MW is easily detected through a change of sign in the slope of the salinity–depth relationship, which typically begins at neutral density values of 27.3 kg m^{-3} or at depths of about 500–600 m, and corresponds to the salinity increasing back above 35.7. At deeper levels, in the 1700–1800 m depth and 27.90 – 27.93 kg m^{-3} density range, the presence of MW disappears. These characteristics are easily appreciated in the temperature–salinity (T – S) diagrams (Fig. 4).

3. Results

Figs. 5–8 present co-located seismic and oceanographic data. Characteristic features in the seismic sections are labeled by their section name (3, 5, 9 or 11) and a corresponding letter. We now present a brief description of these sections and the way they are partitioned using both seismic and oceanographic criteria.

3.1. Partition of seismic lines

Each seismic line is divided using both oceanographic and seismic criteria. The oceanographic partition into three principal zones is based on the presence of MW, which is brought by the MU either via advection or lateral and vertical diffusion. Zones 1 and 3 comprise pure NACW and NADW water masses, respectively, while Zone 2 includes all MW as well as the transitions between it and the overlying and underlying NACW and NADW. To establish this zonation we use a very simple criterion that intermediate waters with salinity above 35.7 have a significant contribution from MW and hence define Zone 2. Waters above and below correspond to Zones 1 and 3, respectively. In general, Zone 1 comprises waters between 0 and 600 m, Zone 2 between 600 and 1600 m and Zone 3 from 1600 m to the seafloor. The width of Zone 2 decreases with distance from the Strait of Gibraltar.

In order to have a comparable seismic partition in three zones we define the MW (Zone 2) based on the root mean square (rms) amplitude of seismic traces. Where this amplitude increases by a factor of five or more, we interpret this to represent the relatively high acoustic impedance of the MW. Amplitudes above and below

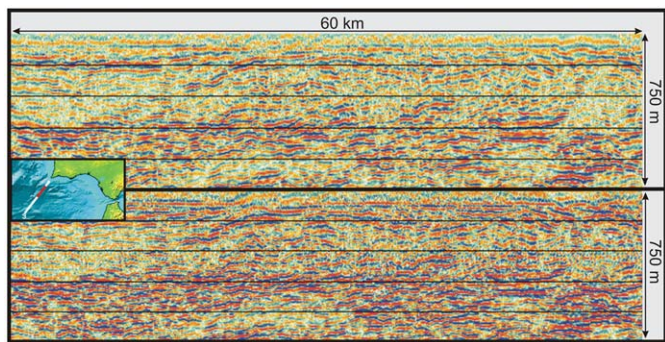


Fig. 3. Comparative results of semblance velocity (sound speed) analysis for a section of line IAM-3 (red, inset). Upper panel stacked with a constant sound speed of 1505 m s^{-1} . Lower panel stacked using a carefully picked temporally and spatially varying sound speed function. Note the better imaged reflections and improved structural clarity, especially in the shallow ocean.

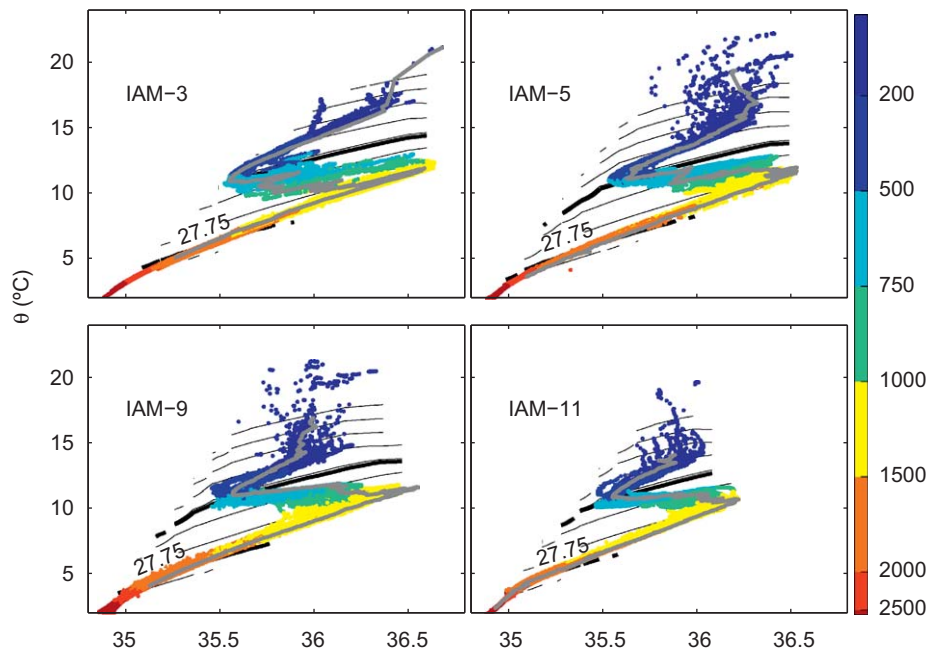


Fig. 4. T–S profiles for the co-located oceanographic sections. Depths (m) are indicated by colors. Isopycnals increase upward, with 0.25 kg m^{-3} intervals. The 27.3 and 27.93 isopycnals, which grossly delimit MW, are drawn as thick black lines. The gray line corresponds to an MW core station.

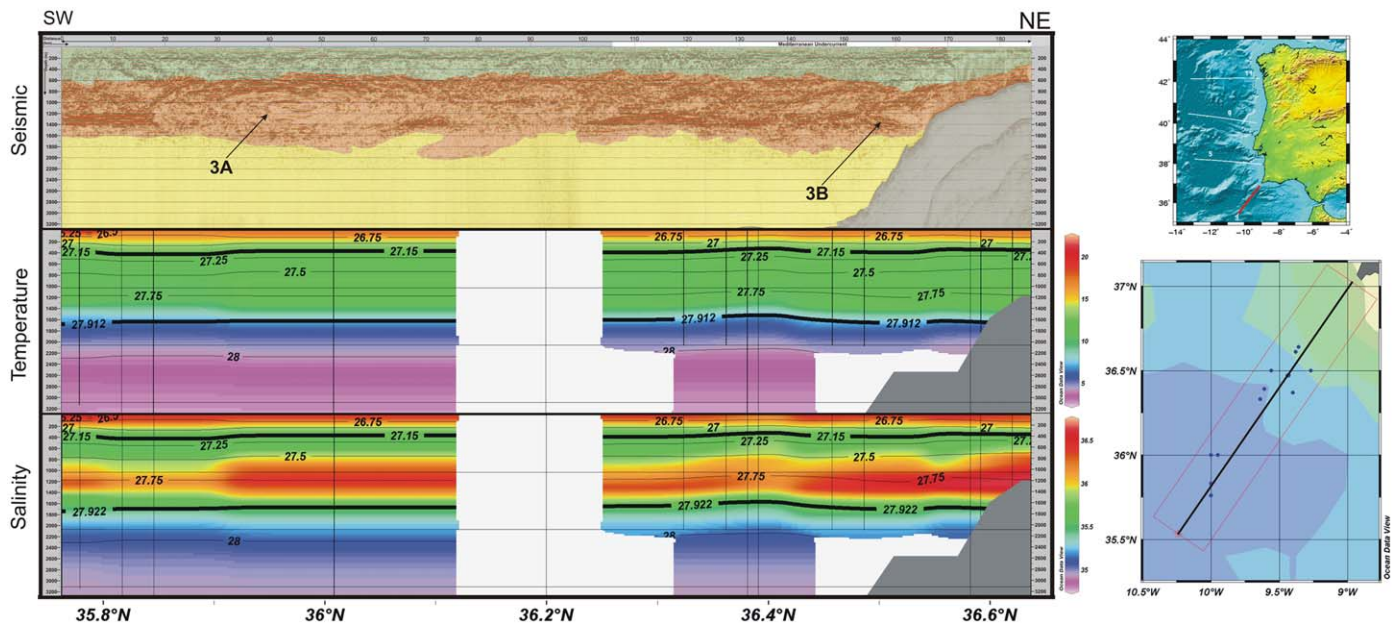


Fig. 5. Co-located seismic (line IAM-3) and historical oceanographic data. Zone 1 (NACW): green. Zone 2 (MW): red. Zone 3 (NADW): yellow. Seafloor: gray. MU is labeled on the top right of sections in white. See text for interpretation. Thick black lines in oceanographic data correspond to neutral density isopycnals (kg m^{-3}). Vertical black lines indicate locations of CTD casts with respect to seismic line. Bottom right inset shows location of seismic line relative to CTD casts (points). White zones indicate oceanographic data gaps.

the MW that fall outside this amplitude criterion are defined as either NACW (Zone 1) or NADW (Zone 3). Using this zonation, we overlay our interpretation by using three different colors: green—NACW; red—MW; yellow—NADW. By using these simple criteria a good correlation between the seismic images and the conventional oceanographic data is emphasized.

The seismic section in Fig. 5 is line IAM-3, a 186 km SW-NE line. There is a prominent lens shaped structure (Feature 3A) located at depths between 500 and 1500 m, extending from 17 to 66 km. The structure has high amplitude reflectivity at its top boundary and low amplitude reflectivity at its lower boundary.

The low amplitude reflectivity contrasts starkly with the high amplitude horizontal reflectors present on either side and protrudes approximately 300–400 m below them. Feature 3A also shows moderate-to-high internal concentric reflectivity banding. Between about 78 and 98 km there is a sharp drop in the reflectivity of the lower boundary of Zone 2 (1400–1600 m), below which there are some lower amplitude sub-horizontal reflections extending to about 2000 m depth, notably deeper than the high amplitude adjacent horizontal reflectors. The north-east side of IAM-3 displays distinct lateral reflection continuity in Zone 2 and exhibits moderately dipping reflection events near the continental

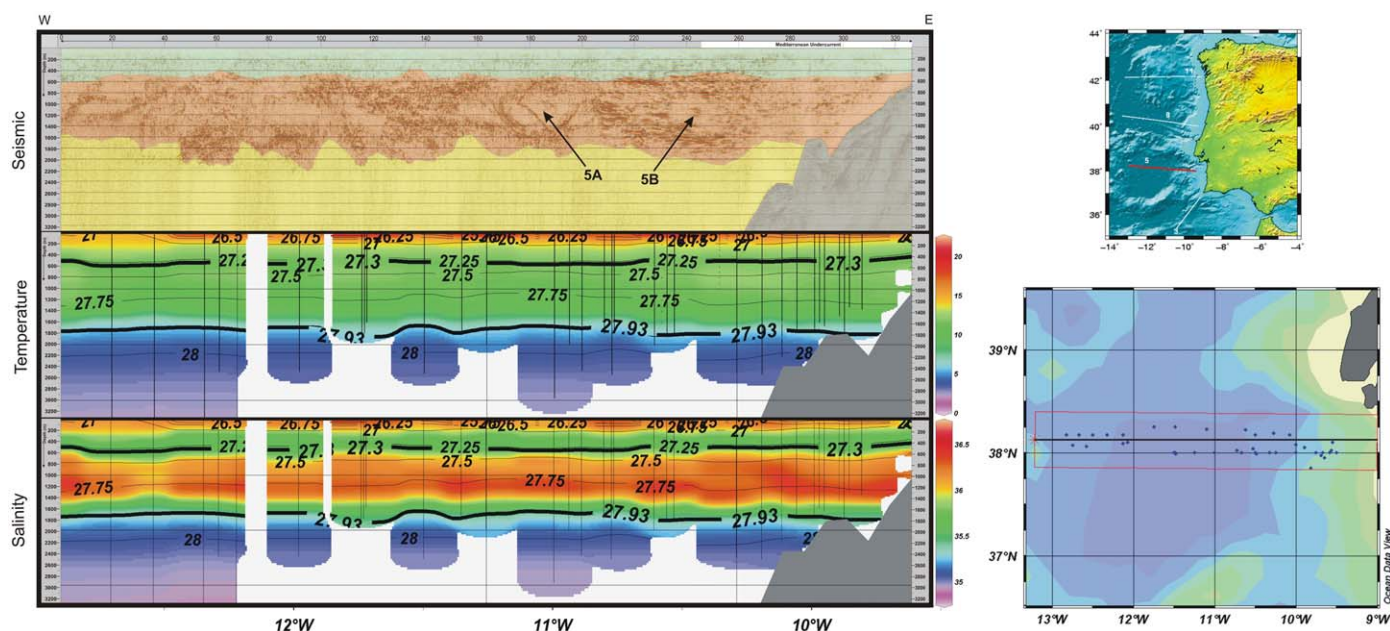


Fig. 6. Caption as in Fig. 5, but now for co-located seismic (line IAM-5) and historical oceanographic data.

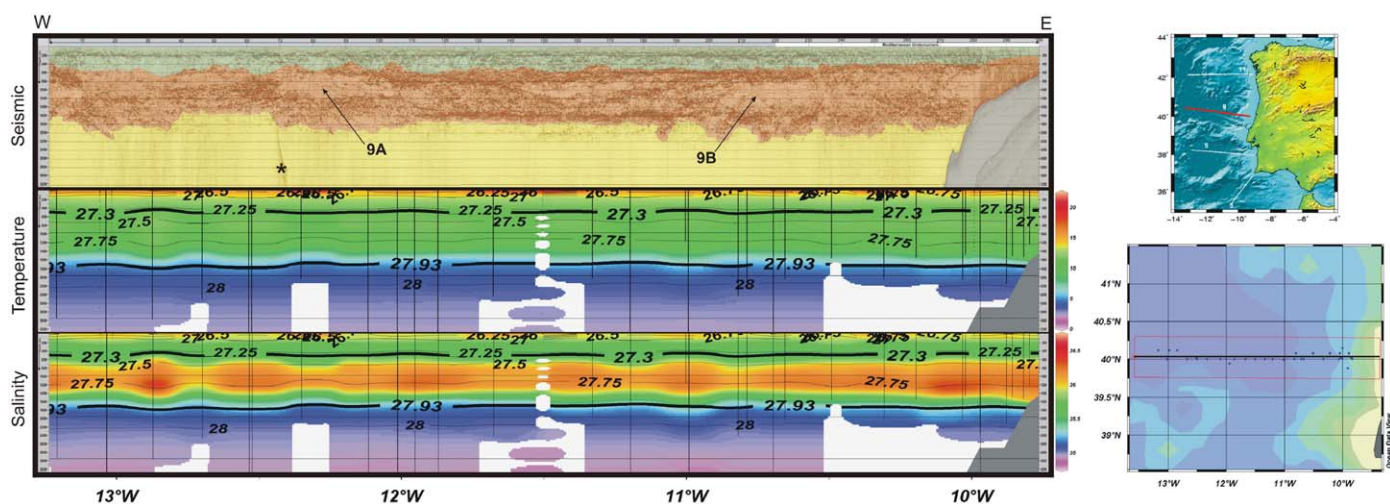


Fig. 7. Caption as in Fig. 5, but now for co-located seismic (line IAM-9) and historical oceanographic data. Asterisk indicates seismic processing artifact.

shelf (Feature 3B). Lateral seismic coherence (reflector lengths) range from 7 to 8 km in some sparse localities to over 60 km long in areas such as the western part of the profile, between 1200 and 1400 m. Zone 3 is largely featureless.

Seismic profile IAM-5 is a 330 km E–W line (Fig. 6). It is characterized by relatively horizontal layers in the upper 400 m (Zone 1). Zone 2 (from 400 to 1600 m) shows long seismic stratification in its easternmost portion (east of 200 km), but this coherency decreases towards the west, so that west of 160 km individual reflectors extend no more than 2–3 km. Two interesting features are noted: Feature 5A, located between 170 and 200 km is a distorted lens-like structure with two apparent cores. Feature 5B, in the eastern part, also appears spherical with low internal reflectivity. Below depths of approximately 1800 m reflectivity diminishes quickly (Zone 3).

Seismic line IAM-9 is a 300 km E–W profile (Fig. 7). Zone 1 contains horizontal reflectors, with maximum continuous lengths of 10 km. Zone 2 clearly exhibits higher amplitude reflections than Zone 1. From 0 to 10 km reflectors are intense and display long lateral continuity. From 10 to 55 km reflectors are

no longer than 2–3 km. Between 55 and 70 km there is an increase in reflection continuity. These lengths increase across the MU, so that between 104 and 230 km we observe high lateral coherence, especially at depths between 1400 and 1700 m, where a single reflector can be traced for 85 km. East of 230 km, approaching the continental shelf, lateral seismic coherence degrades dramatically, with reflectors no longer than 5 km. Seismic features include the pronounced decrease in reflectivity between 600 and 1200 m centered around 84 km (Feature 9A). There are other transparent zones, with little internal structure, such as between 204 km and 235 km (Feature 9B), and between 140 and 170 km. Zone 3 is nearly featureless.

The northernmost line studied is IAM-11, a 220 km long E–W profile (Fig. 8). It shows high amplitude reflectivity with patches of low lateral coherence. At depths corresponding to Zone 1 continuous reflectors can extend up to 30 km, but are nominally between 10 and 20 km long. In Zone 2, in the western part of the profile (from 0 to 50 km) there is high amplitude reflectivity with maximum horizontal reflector lengths of 8 km. From 50 to 80 km and depths between 500 and 1600 m, where the continental shelf

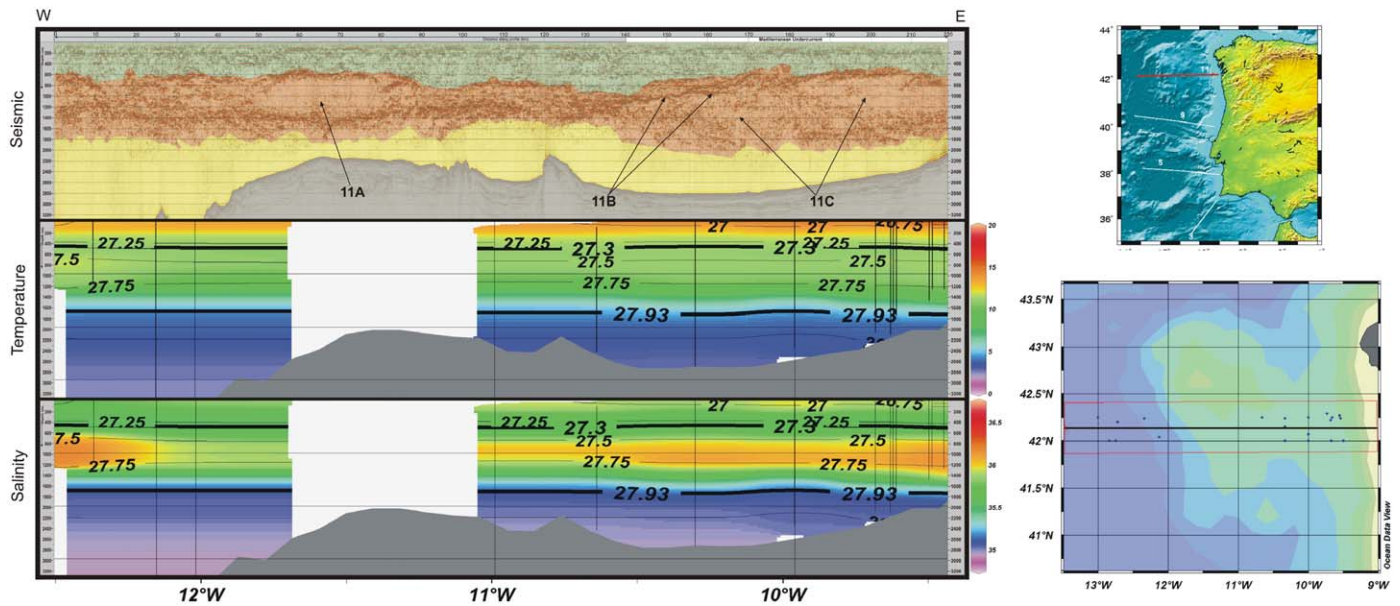


Fig. 8. Caption as in Fig. 5, but now for co-located seismic (line IAM-11) and historical oceanographic data.

noticeably rises, there is a large transparent area (Feature 11A). It is characterized by a high amplitude, relatively horizontally coherent upper boundary that is mimicked directly above (in length and signal strength) by a Zone 1 coherent reflector. Its bottom boundary shows high amplitude signal but is less laterally coherent. Within Zone 2, between 80 and 140 km, there is high amplitude seismic reflectivity but coherent lengths are no more than about 8 km, similar in signal character to the western part of the profile. From 140 km to the continental shelf (approximately 80 km) there are two main features, 11B and 11C. Feature 11B is defined by a high amplitude laterally coherent reflector that moderately rises toward the continental shelf exhibiting reflector lengths up to 20 km. Below this reflector there is a region of low, discontinuous reflectivity (Feature 11C) with sub-horizontal reflectors not longer than 2–3 km. Zone 3, corresponding to depths below 1800 m is highly seismically transparent across the line.

3.2. Seismic amplitude analysis

For display purposes, trace scaling was applied to Figs. 5–8. A trace balance processing algorithm, which applies a single value scalar across all data traces, was selected to preserve lateral amplitude variations and thus improve interpretive potential. However, amplitude contrasts between the seafloor and those internal to the water column are prominent, due to the fact that vertical trace balancing may distort relative amplitudes. Therefore, to further understand the quantitative relationships between the oceanic physical characteristics that influence reflectivity it is necessary to analyze true seismic amplitudes.

Using non-scaled data we calculated the rms seismic amplitude, within a chosen analysis window, for depths corresponding to the Mediterranean Water (500–1500 m; Armi et al., 1989; Richardson et al., 2000). The window locations and dimensions were chosen to coincide with the dominant flow of the MU, within about 80 km of the coast of Iberia (Ambar et al., 1999), while ignoring extremely noisy or clear areas (e.g. near the sea floor and the interior of Feature 5B, Fig. 6). The rms amplitudes are 4.26×10^5 (IAM-3), 3.29×10^5 (IAM-5), 2.71×10^5 (IAM-9) and 1.64×10^5 (IAM-11), a consistent trend of decreasing seismic

amplitude with respect to distance from the source of the MW at the Strait of Gibraltar.

4. Discussion

The MU flows along the south and west coasts of Iberia, from its source in the Strait of Gibraltar (Madelain, 1970). As the MW enters Portimão Canyon at the south coast of Portugal it makes the transition from a density driven bottom current to an intermediate-depth jet, while entraining neighboring water with less momentum (Bower et al., 2002). From Portimão Canyon to Cape St. Vincent a deep and dense continuous MW stream forms (Bower et al., 2002), which is then coerced north along the continental slope by the Earth's rotation. Climatological salinity maps illustrate a high-salinity intermediate-water wedge stretching west of Cape St. Vincent. This is the result of enhanced lateral mixing operating far from the MU through large MW eddies (meddies) (Serra and Ambar, 2002). The MU continues further north along the western coast of Europe, possibly as far as Porcupine Bank (50°N), becoming progressively more diluted (Daniault et al., 1994; Iorga and Lozier, 1999).

4.1. Temperature and salinity fine structure

MW is distinct from the surrounding Atlantic Waters because of its relatively high salinity and temperature values (Ambar et al., 1999). In the Strait of Gibraltar the MU core has a temperature of 13.2°C and a salinity of 38.45, which gives it a density of nearly 1030 kg m^{-3} , more than the underlying NADW (Richardson et al., 1989; Xu et al., 2007). As the MU enters the Gulf of Cádiz it rapidly entrains the neighboring waters and its density decreases until it eventually levels in the $27.7\text{--}27.8 \text{ kg m}^{-3}$ isopycnal range, at the 1000–1500 m depth level. This has a positive anomaly of about 1.0 in salinity and 1.5°C in temperature, as compared with NACW of the same density, which may be redistributed in the form of intermittent steps (fine structure) that become the source of reflectors. These steps consist of nearly constant temperature and salinity values with thicknesses on the order of 10 m (treads in the staircase) that change abruptly over distances of typically 1 m (risers in the staircase).

As the MU moves away from its origin, the temperature, and especially the salinity anomalies become progressively eroded, as is apparent from the T - S diagrams in Figs. 4 and 9. Such a decrease goes together with a reduction in the intensity and number of temperature and salinity steps, and hence in the seismic reflectors seen in the northernmost seismic section (Fig. 8). The erosion of these reflectors along the path of the MU is most probably the result of the interplay between along-stream advection and vertical/horizontal diffusion with the surrounding waters. The evolution of a layer between the MU and the background waters depends on three time scales: (1) an advective time scale T_a , which is the time the MU takes to travel from its Gibraltar source, (2) a vertical diffusive time scale T_v , or the time that the vertical diffusion takes to affect this layer and (3) a horizontal diffusive time scale T_h , the time that this layer takes to laterally incorporate the surrounding properties.

Let us estimate the order of magnitude of these time scales. The diffusive time scale for a layer of thickness h depends on the vertical diffusion coefficient K_v as, $T_d = sh^2/K_v$, where s is a factor that considers the fraction of the property transferred to the adjacent layer (Batchelor, 1977, p. 190). For the MW characteristics to become recognizable we choose $s = 1$, which corresponds to 50% dilution, so that with $K_v \approx 10^{-5} \text{ m}^2 \text{ s}^{-1}$ (as reported by Ledwell et al. (1998), for the eastern subtropical Atlantic) we get $T_d \approx 115$ days for $h \approx 10 \text{ m}$. The horizontal diffusive time scale for a layer $b \approx 30 \text{ km}$ long has a similar dependence on the horizontal diffusion coefficient, K_h , i.e. $T_e = sb^2/K_h$. A sensible choice is $K_h \approx 10 \text{ m}^2 \text{ s}^{-1}$, again from Ledwell et al. (1998), so that $T_e \approx 104$ days ($s = 1$). These two mechanisms tend to erode the layers and compete with its downstream advection. The advective time scale depends on the distance traveled from the region where the temperature and salinity steps were formed. For example, an average current speed of $U \approx 0.1 \text{ m s}^{-1}$ would take a time $T_a = L/U \approx 115$ days to travel a distance $L \approx 1000 \text{ km}$.

Within the MU these diffusive times are probably upper bound estimates, as vertical mixing will be enhanced through bottom friction and vertical shear, while lateral shear will cause enhanced horizontal diffusivity. Furthermore, in some instances the vertical and horizontal diffusive processes will interact such that, in some locations, fine structure may disappear in substantially shorter times. For example, a combined effective diffusive time scale on the order of 10 days implies that layers would not last more than some 100 km as they are advected by the MU.

4.2. Seismic profiles

Fine structure features within the MU are transient. Nonetheless, they have enough spatial and temporal coherence to be imaged by seismic data via strategically located cross-cutting sections of the MU. The coherence and intensity of these seismic reflections not only provide a measure of the sharpness and lateral coherence of the temperature and salinity steps but also draw the bounds of mesoscale structures such as meddies, and the rising/dipping of isopycnals associated with geostrophic currents. Let us now briefly describe some of these features as observed from the processed seismic lines (Figs. 5–8).

We identify the prominent lens shaped structure in IAM-3, Feature 3A (Fig. 5), as a meddy because of its spatial extent (Bower et al., 1997), its location at the depth range predicted by CTD and float surveys (500–1500 m, Armi et al., 1989; Richardson et al., 2000), and the marked horizontal reflection continuity (Chérubin et al., 2003). At the top of the meddy there is a higher than normal amplitude contrast. This agrees with reports of high density contrasts at the top of meddies as the result of lateral intrusions between MW and NACW and double diffusion processes (Biescas

et al., 2008; Serra and Ambar, 2002). An abrupt drop in reflectivity, at about 80 km from the coast, seems to correspond with the western boundary of the MU (Ambar et al., 1999). The north-east side of IAM-3 displays increased lateral reflection continuity but also shows dipping events and areas of lower reflection amplitude (Fig. 5). Notable here is a half lens-shaped structure, 3B, possibly a meddy formed at Cape St. Vincent (Ambar et al., 1999; Serra and Ambar, 2002).

Structures 5A and 5B in IAM-5 (Fig. 6) may represent meddies generated at Cape St. Vincent (Bower et al., 2002; Richardson et al., 2000; Serra and Ambar, 2002). At approximately 200 km, there is a sudden change in signal character, from short-broken reflectors to long-smooth ones. This is likely an artifact due to changes in sea state during seismic recording on either side. The portion from 0 to 200 km (section A offshore) was recorded on 28–29 August 1993. The eastern portion of the line, from 200 to 325 km (section B nearshore), was recorded on 2–3 September 1993. Given that the acquisition parameters were invariant, the difference is most probably due to varying surface conditions at the times of acquisition. Wind speeds were noted on the Beaufort Wind Scale (Ruiz, 1997), of F6 (strong breeze: 41–50 km/h) for section A and F3 (gentle breeze: 13–19 km/h) for section B. As a result wave heights were significantly greater in section A as compared with section B, explaining the discontinuity in signal character and emphasizing the sensitivity of the method to the measurement of environmental conditions. In section A reflectivity and lateral coherence increases toward the coast, pointing to the presence of fine structure reflectors within the MU.

The broken reflectivity observed in the eastern and western parts of IAM-9, such as in Features 9A and 9B, suggests that less fine structure is present (Fig. 7). There are some instances of stable reflections in the central part of the line, but reflectivity appears broken in the nearshore region. This is surprising as the co-located oceanographic data displays a MU core of high salinity, and suggests lateral mixing or intrusions of surrounding water masses. Yet another possibility is that the MU decreases intermittently, for example during the formation of meddies off Cape St. Vincent (Serra and Ambar, 2002).

Profile IAM-11 contains a large lens shaped structure (Feature 11A), a meddy on the basis of its spatial dimensions (Armi et al., 1989; Richardson et al., 2000). Curiously, unlike the meddy from line IAM-3 (Feature 3A), it contains little internal structure (Fig. 8). This suggests an evolution of the meddy interior, which becomes more well mixed as it evolves downstream, resulting in smaller acoustic impedance contrasts and lower reflectivity. Toward the eastern part of the profile, a large sub-horizontal reflector separates NACW and MW (Feature 11B). Below this, a large area of broken reflectivity (Feature 11C) is imaged, suggesting that fine structure layers have less spatial coherence.

4.3. Along-stream changes in seismic reflectors and hydrographic properties

There are abundant seismically imaged mesoscale structures in the MW stratum. In particular, the MU core is easily identified through the rising reflectors against the continental slope, and several meddy-like structures are contoured by long horizontal reflectors. This is in accordance with studies showing increased MW-NACW mixing that occurs as a result of entrainment further away from the source of the MW at the Strait of Gibraltar (Daniault et al., 1994; Iorga and Lozier, 1999; Ochoa and Bray, 1991). However, the MU core displays intermittent reflectivity, which progressively breaks down along its path so that, far from Gibraltar, it becomes nearly transparent. This suggests that the edges of the MU sustain mixing processes, such as double

diffusive vertical mixing and lateral intrusions, prone to result in salinity and temperature staircases, while the MU core is possibly too turbulent to sustain vertical structures. It is possible that these structures are temporally produced through shear-mixing (Pelegri and Sangrá, 1998) but do not appear to last long enough. Therefore, in the core of the undercurrent, the effective vertical and horizontal diffusivities may be substantially larger than at its edge, at least of order $K_v \simeq 10^{-4} \text{ m}^2 \text{ s}^{-1}$ and $K_h \simeq 100 \text{ m}^2 \text{ s}^{-1}$. This would cause the relevant diffusive times (between vertically adjacent layers or between the MU core and the surrounding water) to be shorter than the advective times between adjacent IAM sections, separated by some 200 km.

With the exception of the MU core, the amplitude of seismic reflectors remains maximum within the MW (Zone 2) for all seismic lines. Nevertheless, the rms amplitudes in Zone 2 decrease with distance from the Strait of Gibraltar. We hypothesize that these reflectors are the result of double-diffusion processes, either through diffusive or salt-finger vertical diffusion (on the upper and lower parts of the MW stratum, respectively) or through lateral intrusions. Hence, we may expect that downstream changes in rms seismic amplitudes within the MW are related to changes in salinity and temperature contrasts between the MU and surrounding waters. It could be argued that the observed thermohaline fine structure is the result, to a large degree, of epipycnal (near-horizontal) processes, so that epipycnal contrasts are the most relevant quantities. However, the long-term near-horizontal diffusion of MW is so important that the salinity and temperature contrasts at the MW level are relatively small (Fig. 4), particularly if we are to consider relatively short horizontal distances within the eastern boundary subtropical gyre. Hence, by only considering temperature and salinity values on isopycnals we would likely underestimate the property differences necessary to maintain a long-term and large-scale fine structure field in the whole eastern boundary region. Therefore we believe it is best to consider the properties of the vertically adjacent water masses as they are ultimately responsible for the fine structure in the region, that is the core MW and the deepest NACW.

To calculate the salinity and temperature contrasts we have to define both the MU core and NACW background salinity and temperature values. Here we will use the simplest possible approach for both salinity and temperature. The NACW background salinity is estimated as the minimum salinity value in layers with neutral density less than 27.3 kg m^{-3} (roughly in the top 600 m). The MU core salinity is estimated from data between 27.2 and 27.90 kg m^{-3} (about 500 and 1400 m) in two different ways: (i) directly as the maximum salinity value, and (ii) as the salinity value associated with the maximum temperature value. Similarly, the NACW background temperature is estimated as the temperature corresponding to the minimum salinity value in the top 1000 m. The MU core temperature is estimated from data between 600 and 1400 m in two different ways: (i) directly as the maximum temperature value, and (ii) as the temperature value associated with the maximum salinity value. The NACW and MW data points are shown in Fig. 9 on top of the T - S diagrams for intermediate waters. The salinity, temperature, depth, density and sound speed values are reported in Table 2. When applying the temperature criterion to section IAM-3 we find two cores of MW at different depths, consistent with historical reports of two levels of MW in the western Gulf of Cádiz (Ambar et al., 2002). The two data points are shown in Fig. 9 and the corresponding numbers are reported in Table 2, but thereafter we set the corresponding salinity, temperature and depth values as the average of these pairs of values.

Temperature and salinity contrasts are directly calculated from the NACW and MW temperature and salinity values in Table 2. A plot of rms seismic amplitudes together with salinity and temperature contrasts, as a function of distance (Fig. 10a) does

suggest a direct relation between these quantities. We may appreciate that seismic intensity, as well as salinity and temperature contrasts, decreases along the path of the MU. The precise salinity and temperature contrasts depend on whether we use the maximum salinity (subindex S : ΔS_S , ΔT_S) or the maximum temperature (subindex T : ΔS_T , ΔT_T) criteria, yet both methods show the same tendency. We may further examine if there is a relationship between seismic intensity and the overall salinity and temperature vertical gradients. These gradients are estimated as the property contrast divided by the vertical distance between the corresponding NACW and MW data points, e.g. the salinity contrast attained using the salinity criterion is divided by the vertical distance between the NACW point and the maximum salinity MW point (Fig. 10b). The vertical gradients depend largely on the selected criterion, the gradients being roughly twice as large when using the temperature criterion compared with the salinity criterion. Nevertheless, no matter which criterion, we find that the gradients decrease with distance from the Strait of Gibraltar, roughly paralleling the decrease in seismic amplitude. A linear regression between seismic amplitude and overall vertical temperature gradient gives a slope of 1.2×10^8 with a correlation coefficient of 0.95 when using the salinity criterion and 2.4×10^7 with a correlation coefficient of 0.99 when using the temperature criterion.

These results reinforce the hypothesis that the intensity of the reflectors responds to temperature and salinity vertical differences that favor double-diffusion processes. Yet, we still have not explored two important issues: if one of the two properties, temperature or salinity, has a predominant influence on the presence of these reflectors, and whether the reflectors are mainly controlled by either density or sound speed differences. Let us first explore the latter question. As mentioned in the Introduction, the presence of acoustic reflectors depends on the vertical contrasts of acoustic impedance $I = \rho c$, defined as the product of in situ density ρ and sound speed c . Changes in impedance are given by $\Delta(\rho c) = \rho \Delta c + c \Delta \rho$, such that the relative effect of the two is given by the fraction $(c \Delta \rho) / (\rho \Delta c)$.

The results are reported in Table 3, with subindices S and T referring to the differences obtained using the maximum salinity and temperature criteria, respectively (data in Table 2). The mean sound speed and density contrasts are calculated as the average of the values obtained using both criteria, i.e. $\Delta c = (\Delta c_S + \Delta c_T) / 2$ and $\Delta \rho = (\Delta \rho_S + \Delta \rho_T) / 2$. Notice that to compute the last column we use mean speed and density values calculated simply as the average between core MW and deep NACW values. In order to avoid having differences induced by the overwhelming pressure effect we use one single reference pressure, taken to be that corresponding to a depth of 1000 m, a characteristic depth of the MW. Contrasts in sound speed cause a change in impedance which is typically one order of magnitude larger than those changes caused by contrasts in density, although for section IAM-11 the difference reduces to a factor of about 3.5. These results could have been anticipated, as the difference in potential density between NACW and MW is about 0.2 kg m^{-3} while the sound speed difference is of a few m s^{-1} (at the same pressure), so that $\Delta \rho / \rho$ is one order of magnitude less than $\Delta c / c$.

Finally, we may assess the relative effect that salinity and temperature contrasts have on impedance. We may estimate the speed and density changes due to the salinity contrast as $\Delta c(S) = c(S_m, T_b, z_0) - c(S_b, T_b, z_0)$ and $\Delta \rho(S) = \rho(S_m, T_b, z_0) - \rho(S_b, T_b, z_0)$, and the speed and density changes due to the temperature contrast as $\Delta c(T) = c(S_b, T_m, z_0) - c(S_b, T_b, z_0)$ and $\Delta \rho(T) = \rho(S_b, T_m, z_0) - \rho(S_b, T_b, z_0)$, where S_m and T_m correspond to the maximum MW salinity and temperature values, S_b and T_b correspond to the deep NACW salinity and temperature values, and $z_0 = 1000 \text{ m}$ is a characteristic depth of the MW.

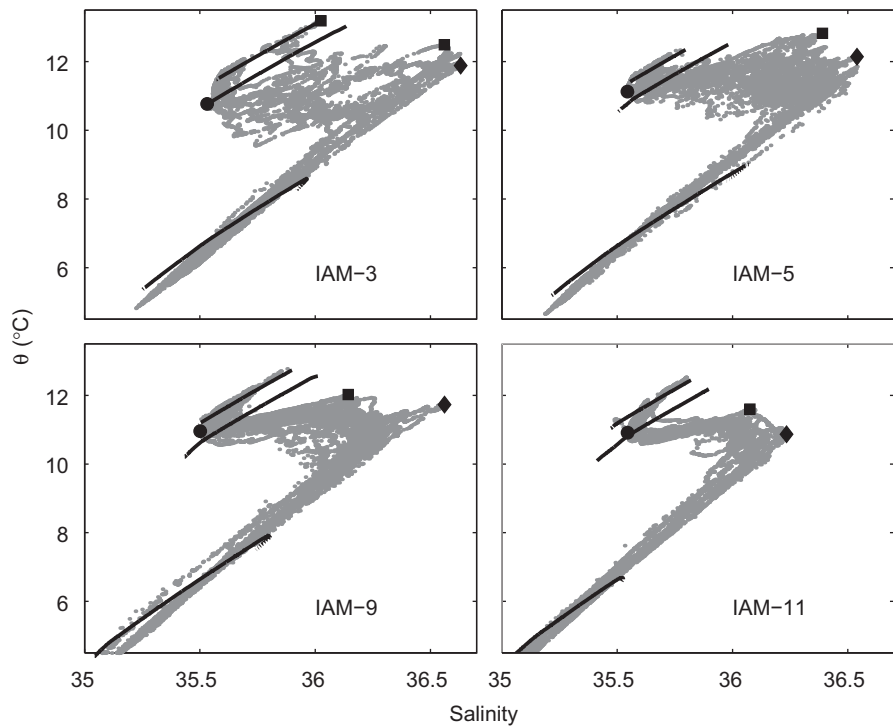


Fig. 9. T–S profiles for the co-located oceanographic data in the MW region, illustrating the criteria used to obtain the background and maximum salinity values. The black lines represent 27.2, 27.3 and 27.9 neutral densities. The dots indicate the background salinity and temperature values, the diamonds show the maximum salinity and temperature values as derived from the maximum salinity criterion, and the squares locate the maximum salinity and temperature values as derived from the maximum temperature criterion. Notice there are two squares in section IAM-3 corresponding to the two MW levels as explained in the text.

Table 2
Salinity, temperature, depth, density and sound speed values.

	MW core (<i>T</i> criteria)			MW core (<i>S</i> criteria)			Deep NACW		
	<i>T</i> _{max} (°C)	<i>S</i> _{max}	<i>z</i> (m)	<i>T</i> _{max} (°C)	<i>S</i> _{max}	<i>z</i> (m)	<i>T</i> (°C)	<i>S</i>	<i>z</i> (m)
IAM-3	13.19	36.03	482.7	11.96	36.62	1176.7	10.77	35.53	555.2
IAM-5	12.83	36.39	733	12.14	36.54	1098.7	11.12	35.54	489.7
IAM-9	12.02	36.14	661.8	11.73	36.56	1383.6	10.96	35.50	428.9
IAM-11	11.60	36.08	790	10.87	36.23	1153	10.91	35.54	427.5
	ρ (kg m ^{−3})		<i>c</i> (m s ^{−1})	ρ (kg m ^{−3})		<i>c</i> (m s ^{−1})	ρ (kg m ^{−3})		<i>c</i> (m s ^{−1})
IAM-3	1031.84		1517.74	1032.29		1515.16	1031.69		1509.72
IAM-5	1031.92		1517.81	1032.19		1515.68	1031.62		1510.96
IAM-9	1031.93		1514.99	1032.29		1514.30	1031.62		1510.36
IAM-11	1031.94		1513.27	1032.21		1510.92	1031.67		1510.22

The results are reported in Table 4, again with subindices *T* and *S* indicating the criterion used to obtain the salinity and temperature differences (Fig. 9). The last column of Table 4 displays the salinity/temperature ratio as obtained using the mean speed contrasts $\Delta c(S)/\Delta c(T) = (\Delta c(S)_T + \Delta c(S)_S)/(\Delta c(T)_T + \Delta c(T)_S)$; in parenthesis we show the range $(\Delta c_S(S)/\Delta c_S(T) \text{ to } \Delta c_T(S)/\Delta c_T(T))$. The results indicate that changes in seismic amplitude are more likely related to temperature than to salinity changes. The mean salinity/temperature ratio varies between 0.20 near the MW source to as high as 0.66 in downstream regions, where salinity contrasts are thus likely to play an increasing (but, still lesser) role in determining thermohaline fine structure. These values agree with recent studies (Nandi et al., 2004; Ruddick et al., 2009) that point to temperature as the major influence on reflection coefficient. Ruddick et al. (2009) obtained a synthetic seismic trace through a meddy located southwest of line (IAM-3) and found

temperature–salinity contributions of 0.83–0.17, giving a salinity/temperature ratio of 0.20.

5. Conclusions

Analysis of four seismic lines acquired as part of the Iberian–Atlantic Margin survey, transecting the Mediterranean Undercurrent, shows distinct seismic reflectors in the upper 1800 m of the ocean. Layering is most prominent from approximately 500 to 1500 m, though this thickness varies from line to line. This corresponds to the base of the North Atlantic Central Water (NACW) and the whole Mediterranean Water (MW) stratum, in many instances with reflectors coherent over distances of over 100 km. Common to all sections is a significant decrease in seismic amplitude between 1400 m and approximately 1800 m, which we interpret as the base of the MW, beyond which North Atlantic Deep Water (NADW) is seismically near-transparent.

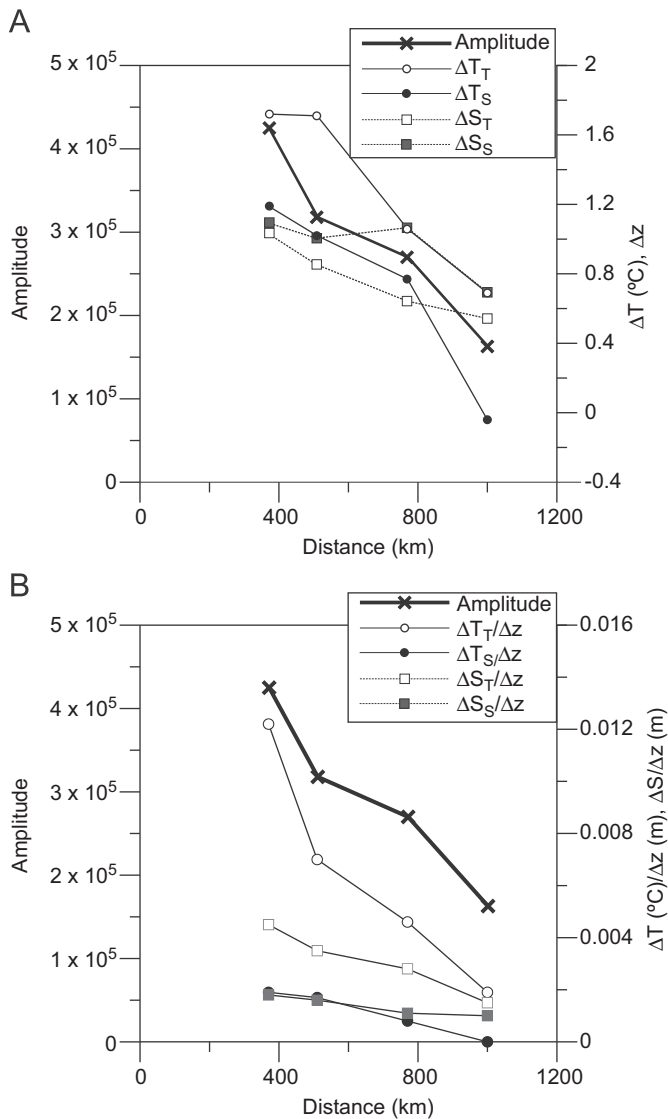


Fig. 10. (A) Decreasing rms seismic amplitudes for the MW and corresponding temperature and salinity contrasts between the MU core and the background NACW, ΔT (solid lines, circles) and ΔS (dotted lines, squares), respectively. We display two different values for the temperature and salinity contrasts, calculated as explained in the text. (B) Seismic amplitude variation alongside the overall vertical temperature and salinity gradients, $\Delta T/\Delta z$ (solid lines, circles) and $\Delta S/\Delta z$ (dotted lines, squares), respectively. In both panels we use the following key. Temperature criterion: empty circles/squares; salinity criterion: filled circles/squares (black: temperature, gray: salinity); rms seismic amplitude: crosses.

Three seismic reflectivity zones are identified, which we associate with NACW, MW and NADW, respectively. The thermohaline spatial structure of NACW and, particularly, MW strata may be studied using seismic oceanography because of the existence of large temperature and salinity contrasts between vertically adjacent water masses. These contrasts translate into gradients of density and sound speed, which bring about impedance gradients and correspondingly large variations in the amplitude of seismic reflectivity. Typical temperature and salinity contrasts between the MU core and the base of the overlying NACW are 1°C and 1, respectively, which lead to (potential) density differences of about $0.3\text{--}0.5\text{ kg m}^{-3}$ and sound speed differences of about $5\text{--}7\text{ m s}^{-1}$. Note that despite the fact that acoustic impedance depends on in situ density, while we look at the role of salinity and temperature contrasts on impedance gradients we must set one single depth in order to remove the overwhelming pressure effect, this is why here we speak of potential density.

Table 3

Sound speed and density contrasts calculated using both the temperature and salinity criteria.

		T criteria				
		$\Delta\rho_T$ (kg m ⁻³)		Δc_T (m s ⁻¹)		
IAM-3		0.22		8.02		
IAM-5		0.30		6.85		
IAM-9		0.29		4.63		
IAM-11		0.27		3.05		
		S criteria				
		$\Delta\rho_S$ (kg m ⁻³)		Δc_S (m s ⁻¹)		
IAM-3		0.60		5.44		
IAM-5		0.57		4.72		
IAM-9		0.67		3.94		
IAM-11		0.54		0.70		
Mean						
		ρ (kg m ⁻³)	$\Delta\rho$ (kg m ⁻³)	c (m s ⁻¹)	Δc (m s ⁻¹)	$(c\Delta\rho)/(\rho\Delta c)$
IAM-3		1031.89	0.41	1513.09	6.73	0.10
IAM-5		1031.84	0.44	1513.86	5.79	0.11
IAM-9		1031.87	0.48	1512.51	4.29	0.16
IAM-11		1031.90	0.36	1511.16	1.88	0.28

Table 4

Sound speed contrasts caused by changes in salinity, $\Delta c(S)$, and temperature, $\Delta c(T)$.

	$\Delta c_S(S)$	$\Delta c_T(S)$	$\Delta c_S(T)$	$\Delta c_T(T)$	$r = \Delta c(S)/\Delta c(T)$
IAM-3	1.33	0.94	4.13	7.11	0.20 (0.32–0.13)
IAM-5	1.21	1.02	3.50	5.81	0.24 (0.35–0.18)
IAM-9	1.28	0.78	2.69	3.68	0.32 (0.48–0.21)
IAM-11	0.84	0.64	−0.16	2.39	0.66 (−5.25 to 0.27)

See text for explanations.

Seismic characterization of the Mediterranean Undercurrent (MU) is found in the reflectivity patterns seen within Zone 2 (MW). The undercurrent is located within some 80 km of the Iberian Peninsula continental slope, as viewed through the rising of reflectors against it, while the MU core remains largely transparent. We interpret these layers of reflectors as representing staircase-type structures induced by double-diffusion processes, which last longer than eroding diffusive processes, while within the MU core the erosion mechanisms dominate.

The analysis of root mean square (rms) amplitudes reveals a decreasing trend of MW seismic amplitude with respect to distance from the Strait of Gibraltar, alongside decreasing temperature and salinity contrasts between MW and the overlying NACW. We deduce that the decrease in seismic amplitude is a result of reduced double-diffusion processes that cannot compete with other diffusive processes that tend to erode the layering. Considering the deepest NACW and the core MW, the latter characterized by the mid-depth temperature maximum, we find a linear relationship between the overall vertical temperature gradient (in $^{\circ}\text{C m}^{-1}$) and the true seismic amplitude with a linear regression slope of 2.4×10^7 . This relation strongly suggests a causal relationship between the intensity of double-diffusion processes, and therefore fine structure, and true seismic amplitude.

Finally, we find that impedance changes are mainly controlled by sound speed changes, as opposed to density contrasts (a factor between 3.5 and 10), and that the speed variations are predominantly caused by temperature rather than salinity contrasts (a factor between 1.5 and 5).

Acknowledgments

The authors would like to extend thanks to the New and Emerging Science and Technology (NEST) initiative of the European Union—The GO Project (NEST-2003-1 adventure), the Spanish Ministry of Education and Science (CGL200404623), GEOCEAN, TOPOIBERIA (CSD2006-00041) and the Generalitat de Catalunya (2005SGR00874) for financial support. Seismic data were processed using ProMAX v.2003, Seismic Unix and Claritas 4.4.1 software. Oceanographic data were analyzed with Matlab and were plotted with Ocean Data View. Finally, we would like to thank Barry Ruddick and an anonymous reviewer for several useful comments which have greatly improved this paper.

References

- Ambar, I., Armi, L.D., Bower, A., Ferreira, T., 1999. Some aspects of time variability of the Mediterranean Water off South Portugal. *Deep-Sea Res.* 46, 1109–1136.
- Ambar, I., Serra, N., Brogueira, M., Cabecadas, G., Abrantes, F., Freitas, P., Gonçalves, C., González, N., 2002. Physical, chemical and sedimentological aspects of the Mediterranean outflow off Iberia. *Deep-Sea Res.* II 49, 4163–4177.
- Armi, L.D., Hebert, D., Oakey, N., Price, J.F., Richardson, P.L., Rossby, H.T., Ruddick, B., 1989. Two years in the life of a Mediterranean salt lens. *J. Phys. Oceanogr.* 19, 354–370.
- Batchelor, G.K., 1957. Symposium on Naval Hydrodynamics, National Academy of Sciences, Washington DC, pp. 409–423.
- Batchelor, G.K., 1977. *An Introduction to Fluid Dynamics*. Cambridge University Press, Cambridge.
- Biescas, B., Sallars, V., Pelegrí, J.L., Machín, F., Carbonell, R., Buffett, G., Dañoibetia, J.J., Calahorrano, A., 2008. Imaging meddy finestructure using multichannel seismic reflection data. *Geophys. Res. Lett.* 35, L11609 10.1029/2008GL033971.
- Bower, A.S., Armi, L.D., Ambar, I., 1997. Lagrangian observations of meddy formation during a Mediterranean Undercurrent seeding experiment. *J. Phys. Oceanogr.* 27, 2545–2575.
- Bower, A.S., Serra, N., Ambar, I., 2002. Structure of the Mediterranean Undercurrent and Mediterranean Water spreading around the Southwestern Iberian Peninsula. *J. Geophys. Res.* 107 (C10), 3161 10.1029/2001JC001007.
- Brandt, A., 1975. Acoustic returns from density fluctuations in turbulent jets. In: *Oceans*, vol. 75. IEEE, New York.
- Candela, J., 2001. Mediterranean water and global circulation. Observing and modelling the global ocean. In: Church, J., Siedler, G., Gould, J. (Eds.), *Ocean Circulation and Climate*. Academic Press, New York, pp. 419–429.
- Chernov, L.A., 1957. Correlation of amplitude and phase fluctuations of a wave propagating in a medium with random inhomogeneities. *Akust. Zh.* 3, 192.
- Cherubin, L.M., Serra, N., Ambar, I., 2003. Low frequency variability of the Mediterranean Undercurrent downstream of Portimão Canyon. *J. Geophys. Res.* 108 (3), 3058 10.1029/2001JC001229.
- Claerbout, J.F., 1978. Snell waves. Stanford exploration project report (15), Stanford University, pp. 57–72.
- Cowen, C.F.N., Grant, P.M., 1985. *Adaptive Filters*. Prentice-Hall, New Jersey.
- Daniault, N., Mazé, J.P., Arhan, M., 1994. Circulation and mixing of Mediterranean Water west of the Iberian Peninsula. *Deep-Sea Res.* 41 (1), 1614–1685.
- Gazdag, J., 1978. Wave-equation migration by phase shift. *Geophysics* 43, 1342–1351.
- Géli, and Cosquer, in preparation.
- Gonella, J., Michon, D., 1988. Ondes internes profondes revelees par sismique reflexion au sein des masses d'eau en atlantique-est, 306.
- González, A., Torné, M., Córdoba, D., Vidal, N., Matias, L.M., Díaz, J., 1996. Crustal thinning in the southwestern Iberia Margin. *Geophys. Res. Lett.* 23 (18), 2477–2480.
- Goodman, L., 1990. Acoustic scattering from ocean microstructure. *J. Geophys. Res.* 95 (C7), 11,557–11,573.
- Hatton, L., Worthington, M.H., Makin, J., 1986. *Seismic Data Processing, Theory and Practice*. Blackwell Scientific Publications, Oxford ISBN: 0-632-01374-5.
- Hauray, L.R., Wiebe, P.H., Orr, M.H., Briscoe, M.G., 1983. Tidally generated high-frequency internal wave packets and their effects on plankton in Massachusetts Bay. *J. Mar. Res.* 41, 65–112.
- Holbrook, W.S., Fer, I., 2005. Ocean internal wave spectra inferred from seismic reflection transects. *Geophys. Res. Lett.* 32, L15604 10.1029/2005GL023733.
- Holbrook, W.S., Páramo, P., Pearce, S., Schmitt, R.W., 2003. Thermohaline fine structure in an oceanographic front from seismic reflection profiling. *Science* 301, 821–824.
- Iorga, M.C., Lozier, M.S., 1999. Signatures of the Mediterranean outflow from a North Atlantic climatology, I, salinity and density fields. *J. Geophys. Res.* 104 (C11(a)), 25,985–26,029.
- Johnson, G.C., Sanford, T.B., O'Neil Baringer, M., 1994. Stress on the Mediterranean outflow plume: part I. velocity and water property measurements. *J. Phys. Oceanogr.* 24, 2072–2083.
- Jones, I.F., Levy, S., 1987. Signal-to-noise ratio enhancement in multichannel seismic data via the Karhunen–Loeve transform. *Geophys. Prospect.* 35, 12–32.
- Ledwell, J., Watson, A., Law, C., 1998. Mixing of a tracer in the pycnocline. *J. Geophys. Res.* 103 (21), 21,499–21,529.
- Machín, F., Hernández-Guerra, A., Pelegrí, J.L., 2006. Mass fluxes in the Canary Basin. *Prog. Oceanogr.* 70, 416–447.
- Madelain, F., 1970. Influence de la topographie du fond sur l'écoulement méditerranéen entre le détroit de Gibraltar et le cap saint-vincent. *Cah. Oceanogr.* 22 (1), 43–61.
- Munk, W.H., Garrett, J.C.R., 1973. Internal wave breaking and microstructure (the chicken and the egg). *Boundary-Layer Meteorol.* 4, 37–45.
- Munk, W.H., Wunsch, C., 1979. Ocean acoustic tomography: a scheme for large scale monitoring. *Deep-Sea Res.* A26, 123–161.
- Nakamura, Y., Noguchi, T., Tsuji, T., Itoh, S., Niino, H., Matsuoka, T., 2006. Simultaneous seismic reflection and physical oceanographic observations of oceanic fine structure in the Kuroshio extension front. *Geophys. Res. Lett.* 33, L23605 10.1029/2006GL027437.
- Nandi, P., Holbrook, W.S., Pearce, S., Páramo, P., Schmitt, R.W., 2004. Seismic reflection imaging of water mass boundaries in the Norwegian Sea. *Geophys. Res. Lett.* 31, L23311.
- Obukhov, A.M., 1941. Scattering of sound in turbulent flow. *Dokl. Akad. Nauk. SSSR* 30, 611–614.
- Ochoa, J., Bray, N.A., 1991. Water mass exchange in the Gulf of Cádiz. *Deep-Sea Res.* 38 (Suppl. 1), S465–S503.
- Orr, M.H., Hess, F.R., 1978. Remote acoustic monitoring of natural suspensate distributions, active suspensate and slope/shelf water intrusions. *J. Geophys. Res.* 83, 4062–4068.
- Ottersten, H., 1969. Atmospheric structure and radar backscattering in clear air. *Radio Sci.* 4, 1179–1193.
- Páramo, P., Holbrook, W.S., 2005. Temperature contrasts in the water column inferred from amplitude-versus-offset analysis of acoustic reflections. *Geophys. Res. Lett.* 32, L24611 10.1029/2005GL024533.
- Phillips, J.D., Dean, D.F., 1991. Multichannel acoustic reflection profiling of ocean water mass temperature/salinity interfaces. In: Potter, J., Warn-Varnas, A. (Eds.), *Ocean Variability and Acoustic Propagation*. Springer, New York, pp. 199–214.
- Pelegrí, J.L., Sangrà, P., 1998. A mechanism for layer formation in stratified geophysical flows. *J. Geophys. Res.* 103, 30679–30693.
- Price, J.F., Baringer, M.O., Lueck, R.G., Johnson, G.C., Ambar, I., Parrilla, G., Cantos, A., Kennelly, M.A., Sanford, T.B., 1993. Mediterranean outflow mixing and dynamics. *Science* 259, 1277–1282.
- Richardson, P.L., Walsh, D., Armi, L.D., Schroder, M., Price, J.F., 1989. Tracking three meddies with float floats. *J. Phys. Oceanogr.* 19, 371–383.
- Richardson, P.L., Bower, A.S., Zenk, W., 2000. A census of meddies tracked by floats. *Prog. Oceanogr.* 45, 209–250.
- Ruddick, B., 1992. Intrusive mixing in a Mediterranean salt lens—intrusion slopes and dynamical mechanisms. *J. Phys. Oceanogr.* 22, 1274–1285.
- Ruddick, B., 2003. Sounding out ocean fine structure. *Science* 301, 772–773.
- Ruddick, B., Gargett, A., 2003. Oceanic double-infusion: introduction. *Prog. Oceanogr.* 56, 381–393.
- Ruddick, B., Kerr, O., 2003. Oceanic thermohaline intrusions: theory. *Prog. Oceanogr.* 56, 483–497.
- Ruddick, B., Song, H., Dong, C., Pinheiro, L., 2009. Water column seismic images as maps of temperature gradient. *Oceanography* 22 (1), 184–197.
- Ruiz, A.L., 1997. *Encyclopedia of the sea (in Spanish)*. Enciclopedias Planeta. ISBN 84-08-01589-3.
- Schmitt, R.W., 1994. Double diffusion in oceanography. *Ann. Rev. Fluid Mech.* 24, 255–285.
- Serra, N., Ambar, I., 2002. Eddy generation in the Mediterranean Undercurrent. *Deep-Sea Res.* II 49, 4225–4243.
- Sheriff, R.E., Geldart, L.P., 1982. *The CMP method of seismic reflection acquisition. Exploration Seismology, History, Theory and Data Acquisition*, vol. 1. Cambridge University Press, Cambridge.
- Stanton, T., Chu, K.D., Wiebe, P.H., 1996. Acoustic scattering characteristics of several zooplankton groups. *ICES J. Mar. Sci.* 53, 289–295.
- St. Laurent, L., Schmitt, R.W., 1999. The contribution of salt fingers to vertical mixing in the North Atlantic tracer release experiment. *J. Phys. Oceanogr.* 29, 1404–1424.
- Tatarski, V.I., 1971. *The Effects of Turbulent Atmosphere on Wave Propagation*. Israel Program for Scientific Translation, Jerusalem, US Department of Commerce Publ., TT-68-50464, pp. 153–162.
- Thorpe, S.A., 2005. *The Turbulent Ocean*. Cambridge University Press, New York ISBN-13 978-0-521-83543-5.
- Treitel, S., 1974. The complex Wiener filter. *Geophysics* 39-2, 169–173.
- Tsuji, T., Noguchi, T., Niino, H., Matsuoka, T., Nakamura, Y., Tokuyama, H., Kuramoto, S., Bangs, N., 2005. Two-dimensional mapping of fine structures in the Kuroshio Current using seismic reflection data. *Geophys. Res. Lett.* 32, L14609 10.1029/2005GL023095.
- Widess, M., 1973. How thin is a thin bed?. *Geophysics* 38, 1176–1180.
- Wood, W.T., Holbrook, W.S., Sen, M.K., Stoffa, P.L., 2008. Full waveform inversion of reflection seismic data for ocean temperature profiles. *Geophys. Res. Lett.* 35, L04608 10.1029/2007GL032359.
- Xu, X., Chassignet, E.P., Price, J.F., Özgökmen, T.M., Peters, H., 2007. A regional modeling study of the entraining Mediterranean outflow. *J. Geophys. Res.* 112, C12005 10.1029/2007JC004145.
- Yilmaz, O., 1987. *Seismic Data Processing*, vol. 2. Society of Exploration Geophysicists.